



Revealing the effects of transition metal doping on CoSe cocatalyst for enhancing photocatalytic H₂ production

Shiwen Du ^{a,1}, Shengqi Lin ^{b,1}, Kuankuan Ren ^b, Chunhe Li ^{b,*}, Fuxiang Zhang ^{a,*}

^a Dalian National Laboratory for Clean Energy, Dalian Institute of Chemical Physics, Chinese Academy of Sciences, Dalian 116023, China

^b Zhejiang Engineering Research Center of MEMS, School of Mathematical Information, Shaoxing University, Shaoxing 312000, China



ARTICLE INFO

Keywords:

Theoretical investigations
Transition metal doping
CoSe cocatalyst
Photocatalytic H₂ evolution

ABSTRACT

Having an insight into the optimizations of intrinsic properties of cocatalysts via doping foreign atoms to promote solar-driven water splitting into hydrogen (H₂) energy conversion is increasingly important, but it remains a challenging scheme. Herein, zero-dimensional/one-dimensional (0D/1D) structured TMCoSe/CdS_{0.95}Se_{0.05} was successfully synthesized through a two-pot hydrothermal treatment. Experimental results show that the FeCoSe/CdS_{0.95}Se_{0.05} photocatalyst exhibits the most excellent photocatalytic H₂ evolution performance (513.76 μmol h⁻¹), which is 36.6 times and 2.0 times higher than that of CdS_{0.95}Se_{0.05} and the optimal CoSe/CdS_{0.95}Se_{0.05}, respectively. In addition, photochemical and photoluminescence results reveal that the FeCoSe/CdS_{0.95}Se_{0.05} sample shows the most rapid carrier dynamics among all samples. Theoretical calculations demonstrate that the excellent activity of FeCoSe/CdS_{0.95}Se_{0.05} nanocomposite can be attributed to the formation of Schottky-type heterojunction between semi-metallic FeCoSe cocatalyst and CdS_{0.95}Se_{0.05}, which can enhance the efficiency of charge carrier separation and utilization, thus promoting the H₂-generation performance.

1. Introduction

Hydrogen (H₂) production from photocatalytic water splitting, as one of the basic reactions in the field of artificial photosynthesis, is considered to be an ideal strategy to effectively alleviate energy crisis and environmental pollution [1,2]. Since the pioneering discovery by Fujishima and Honda in 1972 [3], the photocatalytic water splitting technology mediated by semiconductors has achieved significant development in terms of photocatalysts and H₂ production efficiency during the last few decades [2]. Generally, the photocatalytic water splitting reaction mainly consists of three stages: light absorption, charge separation and migration, and surface redox reaction. And the solar to H₂ conversion efficiency (η_{STH}) is proportional to the efficiencies of these three crucial stages, namely, $\eta_{STH} = \eta_{\text{light absorption}} \times \eta_{\text{charge separation}} \times \eta_{\text{surface reaction}} \times 100\%$ [4]. Therefore, it is necessary to reasonably balance the interrelationship between these factors and implement appropriate strategies to achieve a high catalytic activity in practical research. Although large numbers of semiconductor photocatalysts with wide solar light absorption capacity (e.g., CdS, Ta₃N₅, etc.) have been employed for water splitting, nevertheless, most of them still suffer the problem of low photocatalytic activities. These issues mainly

derive from the short lifetime of photogenerated charges, which will rapidly recombine if not separated and transferred timely [5]. Moreover, the sluggish H₂-generation dynamics of single semiconductors also hamper their practical applications in solar-energy utilization.

Loading suitable cocatalyst is one of the most effective strategies to enhance photocatalytic activities, as it can promote the separation efficiency of photogenerated electron-hole pairs, offer low activation potentials, and serve as active sites for H₂ or O₂ generation [6]. Up to now, tremendous cocatalysts including transition metal carbides, nitrides, oxides, phosphides, and sulfides have been developed and utilized to improve the H₂-evolution activities of semiconductor photocatalysts [7, 8]. Previous literatures report that transition metal selenides (TMSes) can facilitate charge transfer during the H₂ evolution reaction (HER) process, due to their low intrinsic electrical resistivity, and the H adsorption free energy of selenium (Se) site is similar to that of noble metal Pt [9,10]. These advantages signify that TMSes can be potentially served as ideal candidate cocatalysts to boost the photocatalytic HER activities, which has been verified by recent studies. For instance, Yu et al. developed an unsaturated Se-enriched WSe_{2+x} amorphous nanoclusters as cocatalyst to enhance the HER performance of TiO₂, and claimed the enriched Se sites can induce the production of numerous

* Corresponding authors.

E-mail addresses: chunhe@whu.edu.cn (C. Li), fxzhang@dicp.ac.cn (F. Zhang).

¹ These authors contributed equally to this work.

electron-poor Se^{(2-δ)-} to facilitate the adsorption of H_{ads} for fast H₂ formation *via* reinforcing the weak Se–H_{ads} bonds [10]. Sathish and coworkers synthesized nanosized NiSe₂ particles *via* a supercritical fluid process and used them as cocatalyst for TiO₂ to improve the photocatalytic H₂ production rate [11]. Fang et al. fabricated CoSe₂ nanobelts on Se-doped CdS nanowires to achieve an enhanced photocatalytic H₂ generation activity under visible-light irradiation [12]. Besides, other TMSes (e.g., MoSe₂ [13], Cu₂Se [14], NiSe₂ [15], CoSe [16], etc.) have also been employed as outstanding cocatalysts to enhance the photocatalytic H₂ production performance of photocatalysts. Nonetheless, the works on these TMSes cocatalysts usually focused on their promotions for photocatalytic H₂-evolution performances of semiconductors, especially from the perspective of the surface reactivity of cocatalysts. Contrastingly, the internal mechanisms of how TMSes affect interfacial charge spatial separation, and how the synergistic effect between interfacial charge spatial separation and cocatalyst surface reactivity affects the final activity of the catalytic system, have not been clearly demonstrated. In addition, several shortcomings arising from the intrinsic properties of these TMSes cocatalyst are still unsolved, such as (i) undesirable Gibbs free energy (ΔG_{H^*}) for H₂ evolution, (ii) lack of proper structure to establish strong connection with photocatalysts, and (iii) unsuitable energy level within cocatalyst for fast interfacial charge transfer. Therefore, it is highly desirable to develop novel TMSes cocatalyst that can avoid these problems mentioned above. Among various tactics, heteroatom doping is an effective solution, which has been verified to improve the intrinsic properties of cocatalysts such as transition metal sulfides [17,18], nitrides [19,20], etc. To the best of our

knowledge, the effects of dopant on the intrinsic characteristics of TMSes to tailor them with the functions of high-efficiency cocatalysts are still rarely investigated.

In this work, density functional theory (DFT) calculations were first performed to examine the effects of CoSe cocatalyst doped with different transition metal (TM, TM = Mn, Fe, Ni, Cu) ions on visible-light-driven photocatalytic H₂ generation over Se-modified CdS photocatalyst (CdSSe). Based on theoretical investigations, CoSe cocatalyst doping with different TM atoms (abbreviated as TMCoSe) was loaded on CdSSe nanowires (NWs) to fabricate TMCoSe/CdSSe hybrid photocatalyst *via* facile solvothermal treatment. It is revealed that the H₂ evolution activity of CdSSe can be enormously increased with different degrees by loading TMCoSe cocatalyst.

2. Experimental section

2.1. DFT calculations

All the first-principles calculations in this work were performed by using the Vienna Ab-initio Simulation Package (VASP) [21,22] based on the density functional theory. In the calculations, the projector augmented wave (PAW) method [23,24] was utilized to deal with the interaction between valence electrons and ions. The cutoff energy of the plane wave was set at 500 eV, and the generalized gradient approximation (GGA) [25] in Perdew-Burke-Ernzerhof (PBE) [26] form was used to describe the exchange correlation function. According to the Monkhorst-Pack [27] scheme, the bulk CdS_{0.95}Se_{0.05} (abbreviated as

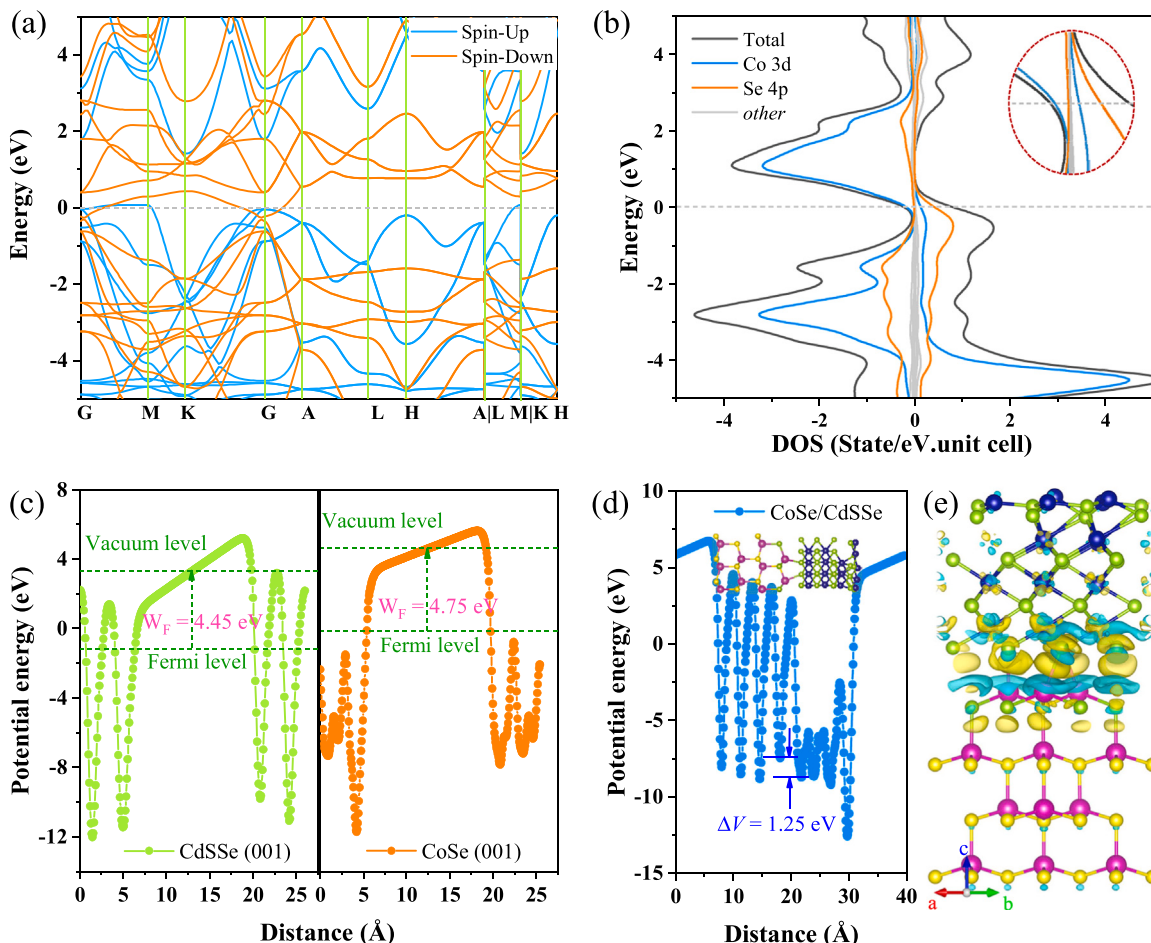


Fig. 1. (a) Band structure and (b) PDOS of bulk CoSe; W_F of (c) CdSSe, CoSe slabs, and (d) CoSe/CdSSe heterostructure; (e) EDD of CoSe/CdSSe heterostructure with an isosurface value of $1.5 \times 10^{-3} \text{ e}^{-3} \text{ Å}^{-3}$ (yellow and blue parts indicate the aggregation and depletion of the electron). The yellow, magenta, green, and mazarine balls represent S, Cd, Se, and Co atoms, respectively.

CdSSe) and CoSe were sampled using $5 \times 5 \times 3$ and $9 \times 9 \times 5$ k -point grids in the Brillouin zone, respectively. In the process of structure optimization, all atoms were fully relaxed, and the energy convergence threshold was 1.0×10^{-5} eV. The force convergence threshold of each atom was $0.015 \text{ eV}\cdot\text{\AA}^{-1}$. The fully relaxed lattice parameters for CdSSe and CoSe are summarized in Table S1. The models of TM heteroatom (TM = Mn, Fe, Ni, or Cu) doped CoSe were built based on a CoSe $2 \times 2 \times 2$ supercell (illustrated in Fig. S1) to investigate the effects on the electronic structure properties on CoSe, and the k -point grids was set as $4 \times 4 \times 3$. PBE + U approach was employed to accurately describe the Mn 3d, Fe 3d, Co 3d, Ni 3d, Cu 3d, and Cd 4d electron states, and the U values for these d states were chosen to 3.9 eV, 3.0 eV, 4.0 eV, 5.0 eV, 4.0 eV, and 4.0 eV according to the previous reports [14,16,28–31], respectively.

In order to identify the difference in intrinsic electronic properties between CdSSe catalysts and cocatalysts, the periodic slabs with four layers for CdSSe (001), CoSe (001), TMCoSe (001) facets, and TMCoSe/CdSSe heterostructure, which was constructed based on the CdSSe (001) $\sqrt{3} \times \sqrt{3} \times 1$ supercell and CoSe (001) $2 \times 2 \times 1$ supercell slabs (Fig. S2) with a lattice mismatch of 3.7%, were built with a vacuum spacing of 15 Å and a k -point grid of $4 \times 4 \times 1$, respectively. The work function (W_F) was given by Eq. (1) (E1):

$$W_F = E_V - E_F \quad (1)$$

where the E_V and E_F are denoted as the electrostatic potentials of the vacuum and Fermi energy levels of the semiconductor, respectively. The Gibbs free energy of hydrogen absorption (ΔG_{H^*}) was calculated with a corrected formula as follows in Eqs. (2 and 3) (E2 and E3) [32]:

$$\Delta G_{H^*} = \Delta E_H + 0.24 \text{ eV} \quad (2)$$

$$\Delta E_H = E_{\text{slabs+H}} - E_{\text{slabs}} - 1/2 E_{H_2} \quad (3)$$

where $E_{\text{slabs+H}}$, E_{slabs} , and E_{H_2} refer to the total energy of slabs with an H atom absorbed, the total energy of slabs, and the total energy of an H_2 molecule in the gas phase, respectively.

2.2. Catalysts preparation

All chemical reagents are of analytical grade and used as received without further purification.

2.2.1. Synthesis of CdSSe NWs

$\text{Cd}_{0.95}\text{Se}_{0.05}$ (CdSSe) NWs were prepared via a facile solvothermal and anion exchange method [12].

2.2.2. Synthesis of CoSe/CdSSe NCs

CoSe/CdSSe nanocomposites (NCs) were synthesized as follows: A certain amount of $\text{Co}(\text{NO}_3)_2 \cdot 6 \text{ H}_2\text{O}$ and SeO_2 were dispersed into 1 mL deionized water under ultrasonication, and then slowly added into 65 mL ethylene glycol containing dispersed 1.5 mmol CdSSe NWs. After stirring for 30 min, the mixture was transferred into a Teflon-lined autoclave and maintained at 180 °C for 12 h. After cooling to room temperature, the resulting solid products were washed with deionized water and ethanol several times, and dried at 60 °C overnight. The obtained samples containing different CoSe loading amounts (Co/Cd = 20%, 30%, 40%, and 50%) were marked as $x\%$ -CoSe/CdSSe accordingly.

2.2.3. Synthesis of TMCoSe/CdSSe NCs

TMCoSe/CdSSe NCs were prepared by the method similar to $x\%$ -CoSe/CdSSe NCs, except that a certain amount of TM nitrate was added into the $\text{Co}(\text{NO}_3)_2 \cdot 6 \text{ H}_2\text{O}$ and SeO_2 aqueous solution (TM/Cd = 10 mol%, TM = Mn, Fe, Ni or Cu). The obtained samples containing different TM dopants were marked as TMCoSe/CdSSe accordingly.

2.3. Catalysts characterizations and photocatalytic (photoelectrochemical) tests

Full details of the characterizations, photocatalytic H_2 production and photoelectrochemical tests are described in the Supporting Information.

3. Results and discussion

3.1. DFT explorations

Electronic band structure of pristine CoSe illustrated in Fig. 1a shows substantial electronic states (Co 3d and Se 4p, Fig. 1b) across the Fermi level (E_F), indicating the inherent metallic characteristics of the CoSe, which would favor the electron transfer in catalysis [16]. Apart from extraordinary conductivity, a highly active cocatalyst must efficiently and unidirectionally extracts the photogenerated electrons from the photocatalyst (e.g., CdSSe in this work), and delivers them to its surface. Work function (W_F) is considered to be a crucial factor in assessing the capability of a metal-/semimetal-based cocatalyst to capture photogenerated carriers [33]. As shown in Fig. 1c, the W_F of CoSe was calculated to be 4.75 eV, which was higher than that of CdSSe (4.45 eV). The difference in the W_F between the CoSe and CdSSe indicates that a Schottky-type heterojunction can be constructed when they are in close contact with each other. This can be further confirmed by charge density difference (CDD) analysis. Fig. 1e depicts the calculated CDD of

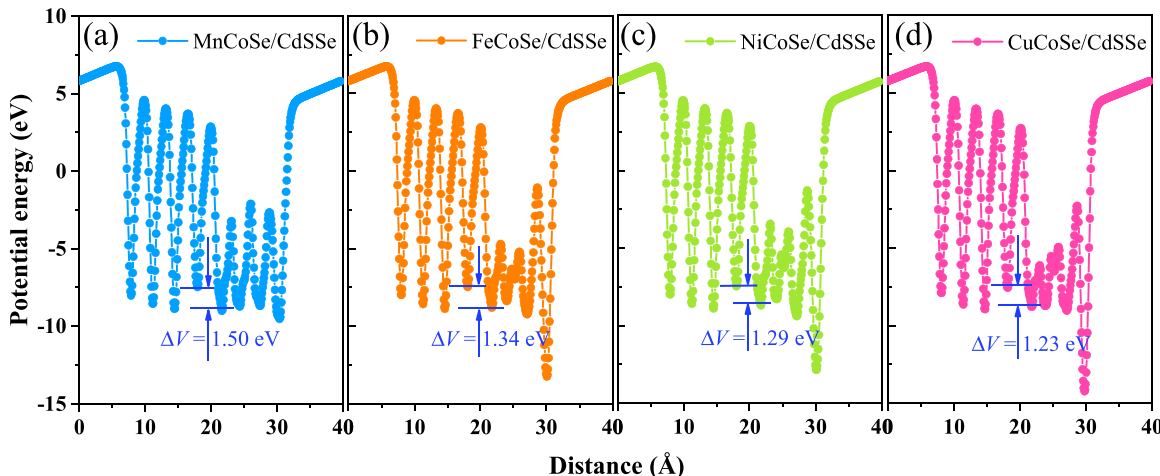


Fig. 2. Calculated potential drop of (a) MnCoSe/CdSSe, (b) FeCoSe/CdSSe, (c) NiCoSe/CdSSe, and (d) CuCoSe/CdSSe heterostructure, respectively.

CoSe/CdSSe heterostructure, in which the charge redistribution happens at the interface region. This manifests the electrons can transfer from CdSSe side to the CoSe side (quantified as 0.5145 electrons/unit model via Bader charge calculations) across the interface, resulting in the upward bending of the conduction band (CB) of CdSSe to form Schottky barrier. Ultimately, the electron transfer from the metallic CoSe to the CB of CdSSe would be suppressed owing to the formed Schottky barrier at the interface [34]. Moreover, there is a large potential drop (ΔV) of 1.25 eV across the interface of the CoSe/CdSSe Schottky heterostructure along the vacuum layer (Fig. 1d). The potential drop at the heterojunction interface can induce a large built-in electric field from CoSe to the CdSSe portion, which could act as a driving force to facilitate the separation rate of photogenerated electron-hole pairs by propelling them to different portions of heterostructure during the photocatalytic process [35].

As shown in Fig. S3, no additional band gaps appear around the Fermi energy level after doping with TM ions, indicating that the metallic characteristics can be inherited for these TMCoSe. This is mainly because of the similarities between cobalt and TM elements, especially the ionic radii and bonding properties. Moreover, the partial density of states (PDOS) around the E_F of TMCoSe is more intensive than that of pure CoSe, especially FeCoSe. This demonstrates that embedded TM heteroatom can reinforce hybridization between Co 3d and Se 4p orbitals, thus significantly enhancing the intrinsic conductivity of the material [36]. The W_F of TMCoSe can be identified in the range of 4.70 ~ 4.86 eV (Fig. S3), which all are higher than that of CdSSe (4.45 eV). These results illustrate the Schottky barrier can be formed when TMCoSe is in contact with CdSSe, which is similar to the CoSe/CdSSe analyzed above. Generally, a high W_F difference can result in significant surface band bending with respect to the Schottky barrier, which can effectively prevent the backflow of photogenerated electrons [37]. In the present work, FeCoSe and NiCoSe exhibit much higher W_F compared with CdSSe. This means that a sufficiently high Schottky barrier could be formed in the CB of CdSSe for TMCoSe/CdSSe heterojunctions, which could effectively inhibit the return of excited electrons from TMCoSe cocatalyst to CdSSe. Furthermore, large ΔV across the interface of the TMCoSe/CdSSe heterostructures was also noted as presented in Fig. 2. Specifically, ΔV values of the MnCoSe/CdSSe and FeCoSe/CdSSe heterostructures are 1.50 eV and 1.34 eV, respectively, which are both higher than that of CoSe/CdSSe (1.25 eV), implying the two heterojunctions have stronger driving force of charge carrier separation than CoSe/CdSSe. These results analyzed above demonstrate doping TM ions has obvious effects on the electronic structure of CoSe and target TMCoSe/CdSSe heterostructures, especially for MnCoSe/CdSSe and FeCoSe/CdSSe hybrid structures. As a result, carrier migration and spatial separation in these heterostructures can be significantly increased, thus achieving high charge separation efficiency ($\eta_{\text{charge separation}}$) of the photogenerated electron-hole pairs.

Theoretically, an effective cocatalyst should possess the ability not only to enhance the charge separation efficiency of carriers, but also to accelerate the surface HER rate. Therefore, to evaluate the catalytic activities of different target TMCoSe cocatalysts in the HER, the Gibbs free energies of hydrogen adsorption (ΔG_{H^*}), a known descriptor of catalysts for the H₂ evolution step [38], were calculated. Here, the (101) surface was chosen as the adsorption surface, as it has been frequently observed in CoSe material [36,39], and both TM and Se sites can coexist on this surface. Prior to investigating the effects of doping with different TM ions on the free energies of CoSe, suitable hydrogen adsorption sites for ΔG_{H^*} calculations were considered deliberately, as illustrated in Figs. S5 and S6. Calculated results suggest that the Se centers are the active sites of the HER rather than the metal (Co) site in CoSe (Fig. S7a), as it shows a lower $|\Delta G_{H^*}|$ value (0.15 eV) than Co site (-1.73 eV), which is similar to other selenides reported previously [40,41]. After being doped with Fe element, the $|\Delta G_{H^*}|$ value for the Se site nearby the doped Fe atom (-0.03 eV) decreases distinctly, demonstrating the positive effect of Fe doping. However, the exposed Fe atoms combined

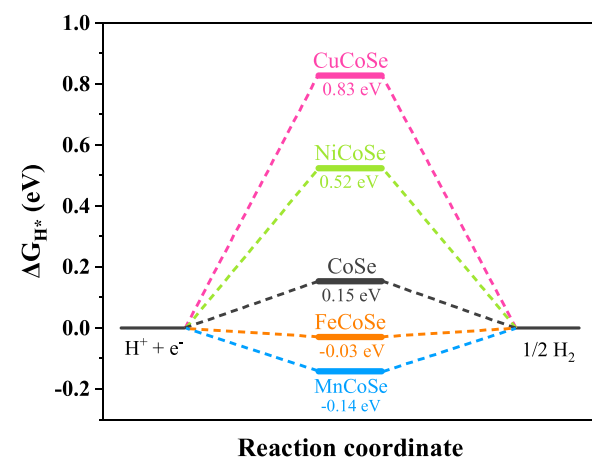


Fig. 3. Free energy diagram for hydrogen adsorbed on Se site nearby TM atom in different TMCoSe structures.

with the H atom exhibit a larger ΔG_{H^*} value of -1.94 eV (Fig. S7b), indicating that Fe atoms are not active sites but can only effectively change the electronic state density of Se and Co atoms in FeCoSe. The ΔG_{H^*} based on Se site adsorption for other TMCoSe materials was subsequently calculated. As exhibited in Fig. 3, compared with pure CoSe, doping the elements with smaller atomic number than cobalt (e.g., Mn and Fe) in the periodic table will enhance the adsorption of hydrogen atoms (gives more negative ΔG_{H^*}), while doping the elements with larger atomic number (e.g., Ni and Cu) will weaken the adsorption (gives more positive ΔG_{H^*}). These variations could be attributed to the charge redistribution after TMs being doped on CoSe, which can be verified by the electron localization function (ELF) plots of Co, Se and TM atoms in TMCoSe as presented in Fig. 4. In principle, too positive or too negative of ΔG_{H^*} is detrimental to HER, since H^{*} cannot efficiently absorb on the catalyst or desorb from the catalyst, respectively [38]. It can be seen from Fig. 3 that the ΔG_{H^*} value of FeCoSe (Se site, -0.03 eV) is lower than that of other CoSe-based catalysts (optimized structures are depicted in Fig. S8), indicating its excellent surface catalytic HER activity.

The results analyzed above give that the electronic structure properties of CoSe and CoSe/CdSSe heterostructure can be optimized by doping with foreign TM elements. Particularly, doping with Mn or Fe element, especially Fe element, would not only induce the formation of a strong built-in electric field at the interface of TMCoSe/CdSSe to accelerate the separation of electron-hole pairs to achieve high $\eta_{\text{charge separation}}$, but also significantly reduce the ΔG_{H^*} to improve the surface HER efficiency ($\eta_{\text{surface reaction}}$). Hence, it is reasonable to expect that the two TMCoSe materials could function as efficient HER cocatalysts to boost the photocatalytic H₂ production over CdSSe photocatalyst. Nonetheless, MnCoSe/CdSSe gives a higher ΔV than FeCoSe/CdSSe (1.50 eV vs. 1.34 eV), while FeCoSe presents a lower ΔG_{H^*} than MnCoSe/CdSSe (-0.03 eV vs. -0.14 eV). Which TMCoSe/CdSSe (TM = Mn or Fe) heterojunction has the superior H₂ generation activity under the same evaluation conditions is still in doubt. Therefore, it is necessary to execute verification experiments to reveal these problematical synergistic effects between $\eta_{\text{charge separation}}$ and $\eta_{\text{surface reaction}}$ originating from foreign TM atom doping.

3.2. Analysis and discussion of experimental result

3.2.1. HER activities and microstructures of CoSe/CdSSe NCs

Motivated by the above promising predictions, a series of x%-CoSe/CdSSe NCs were designed, fabricated and used for photocatalytic HER. Fig. S9a shows the photocatalytic H₂ production amount over CdSSe and x%-CoSe/CdSSe NCs. Obviously, pure CoSe is inert for H₂ production due to its metallic properties [16], which has been confirmed by the

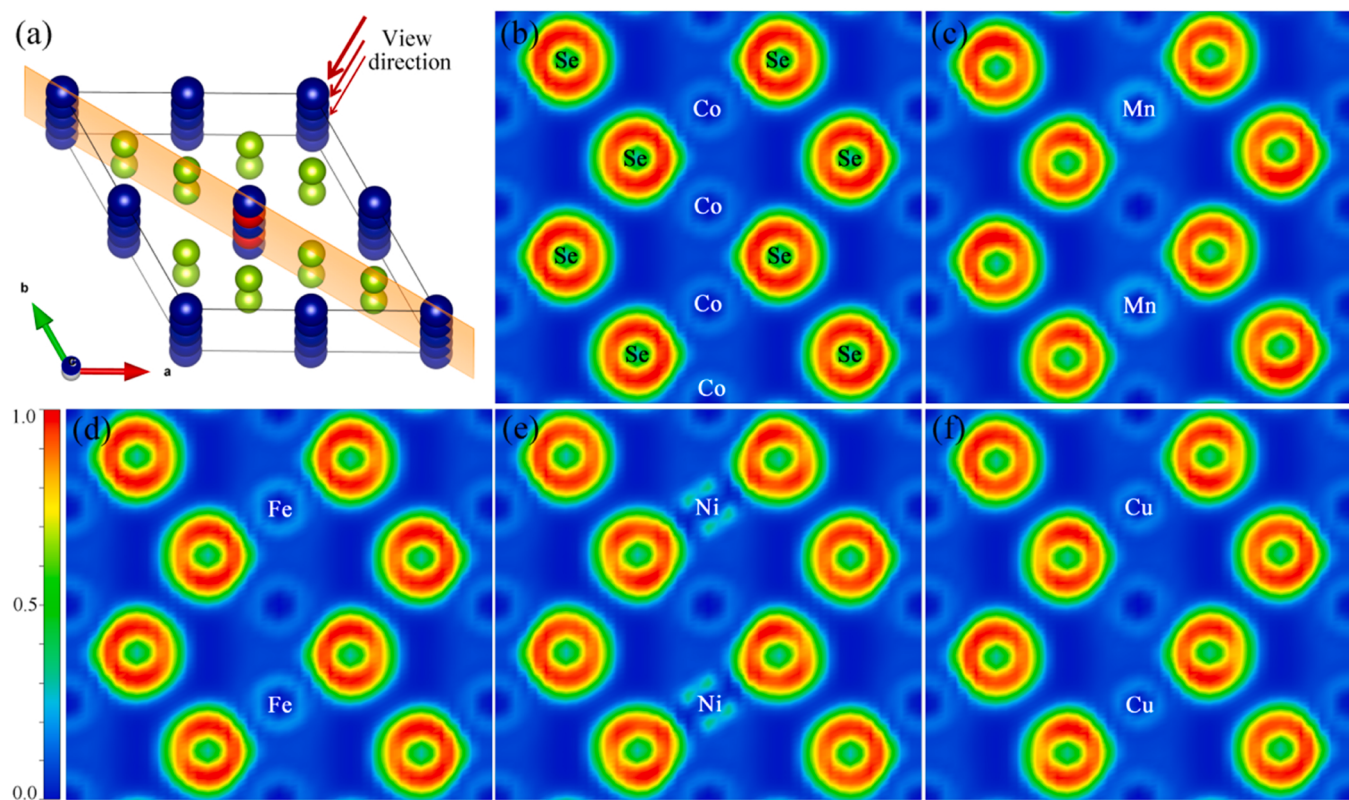


Fig. 4. (a) Crystal structure of TMCoSe, where the blue, green and red balls respectively refer to Co, Se and TM atoms; and corresponding ELF slice mappings of (b) CoSe, (c) MnCoSe, (d) FeCoSe, (e) NiCoSe and (f) CuCoSe, respectively.

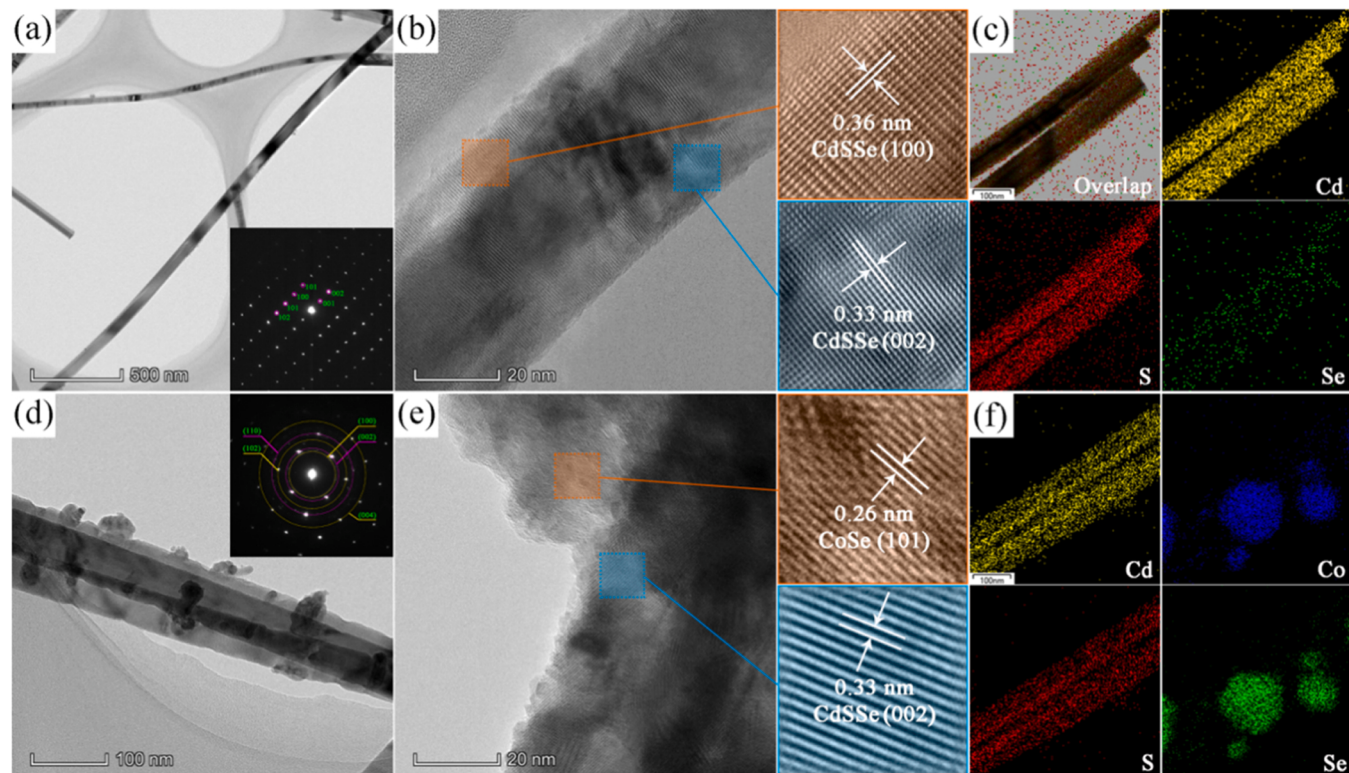


Fig. 5. TEM, HRTEM, and elemental mapping images of (a-c) pure CdSSe NWs and (d-f) 40%-CoSe/CdSSe NC, respectively, and the insets (bottom right in (c) and top right in (d)) show their SAED patterns.

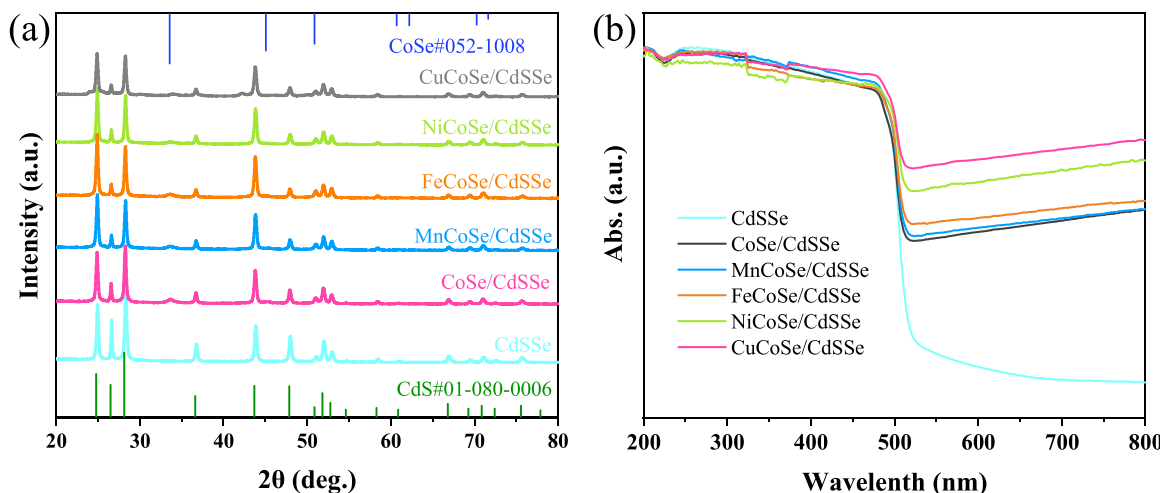


Fig. 6. (a) XRD patterns and (b) UV-vis DRS of the as-prepared samples.

UV-vis diffuse reflectance spectra (DRS) (Fig. S10) and the DOS analysis (Fig. 1b). Blank CdSSe exhibits a sluggish H₂ generation rate of 18.36 μmol/h, which could be ascribed to the high recombination rate of photogenerated electron-hole pairs. Compared with pure CoSe and CdSSe, it should be noted that the H₂ production rate of x%-CoSe/CdSSe NCs is significantly increased. Specifically, 40%-CoSe/CdSSe sample possesses the highest accumulated H₂ production and average H₂ evolution rate (232.34 μmol/h), which is about 12.6 times higher than that of pure CdSSe NWs. When the molar ratio of CoSe and CdSSe is higher or lower than 40%, the HER activity of x%-CoSe/CdSSe NCs is decayed to different degrees. This result shows that loading appropriate CoSe may provide abundant active sites for HER and promote the separation of photogenerated carriers. However, too many or too few loads may result in self-aggregation or deficiency of active sites, which leads to the decreased H₂ production performance.

To understand the influence of structure and morphology on photocatalytic activity, X-ray diffraction (XRD) patterns and transmission electron microscopy (TEM) images of CdSSe, CoSe and x%-CoSe/CdSSe NCs samples were characterized. Fig. S11 shows the XRD patterns of these samples. Obviously, the diffraction peaks of CdSSe are quite similar to those of pure CdS without doping Se element, which can be indexed to the hexagonal phase (JCPDS No. 080-0006), while the peaks of CoSe can be ascribed to the hexagonal phase by comparison with the standard card (JCPDS No. 052-1008). As given in Fig. S11(b), x%-CoSe/CdSSe NCs exhibit the characteristic peaks of CoSe and CdSSe without obvious shift, which confirms that CoSe nanoparticles (NPs) do not grow into the lattice but probably only loaded onto the surface of CdSSe NWs. This is consistent with the DRS exhibited in Fig. S10, which shows a similar absorption spectrum and cutoff absorption edge of x%-CoSe/CdSSe NCs and CdSSe NWs, indicating CoSe does not change the crystal structure of CdSSe [14]. The morphologies of pure CdSSe and 40%-CoSe/CdSSe NCs were investigated by the TEM technique. Fig. 5a shows that CdSSe exhibits a typical one-dimensional nanowire structure with an average diameter of approximately 80 nm and a length of up to micrometers. The distinct interplanar spacing in high-resolution TEM (HRTEM) image (Fig. 5b), e.g., 0.36 nm for (100) facet and 0.33 nm for (002) facet, indicates the high-quality-crystalline hexagonal structure of CdSSe NWs. This can also be verified by the ordered diffraction spots in selected area electron diffraction (SAED) shown in the inset of Fig. 5a. Moreover, the existence and homogeneous dispersion of Se element in CdSSe NWs were confirmed by EDS results shown in Fig. 5c. After loading CoSe onto CdSSe, the image (Fig. 5d) presents a combination of NWs and NPs, and the observed lattice fringes of 0.26 nm in Fig. 5e can be assigned to the (101) plane of hexagonal CoSe. The results of diffraction spots and diffraction rings (inset in Fig. 5d), EDS mapping

(Fig. 5f) and XRD patterns (Fig. S11b) suggest that CoSe NPs are successfully loaded onto CdSSe NWs.

X-ray photoelectron spectroscopy (XPS) of CdSSe and 40%-CoSe/CdSSe NCs were monitored to gain further insight into the surface composition, and the high-resolution XPS spectra are depicted in Fig. S12. The peaks in Fig. S12a at 404.6 eV and 411.4 eV with a difference of 6.8 eV for CdSSe refer to the binding energies (BEs) of Cd 3d_{5/2} and 3d_{3/2}, respectively [14]. And the doublet peaks of S 2p (Fig. S12b) for CdSSe are found at 161.1 eV and 162.3 eV. Meanwhile, the BEs located at 53.4 eV and 54.3 eV could be assigned as Se 3d_{5/2} and Se 3d_{3/2}, respectively [42]. The characteristic peaks of Co 2p are also clearly specified in Fig. S12d with the BEs of 781.2 eV and 796.8 eV for Co (II) 2p_{3/2} and Co (II) 2p_{1/2}, respectively [43]. It is worth noting that the peaks of both Cd 3d and S 2p for 40%-CoSe/CdSSe NCs shift toward higher BEs compared to pristine CdSSe NWs, while the peaks of both Co 2p and Se 3d shift toward lower BEs compared to pure CoSe NPs. Generally, the binding energy is negatively correlated with the surface electron density. These results indicate there is a portion of electrons transfer from CdSSe to CoSe portion when they contacted each other, which is in accordance with the DFT analysis mentioned above. Additionally, it also suggests the strong interaction formed between the interface of CoSe cocatalyst and CdSSe NWs, which is advantageous in improving the photogenerated charges transfer ability.

Combined with the above results, it is found that loading different contents of CoSe on CdSSe to form heterojunctions can improve the photocatalytic activity to different degrees. Especially, 40%-CoSe/CdSSe NCs show the highest photocatalytic activity (Fig. S9). On the basis of screening out the optimal nanocomposite ratio of CoSe and CdSSe, the effects of TM doping on CoSe cocatalyst on the photocatalytic H₂ evolution performance of CdSSe were investigated subsequently. Additionally, hereinafter the 40%-CoSe/CdSSe is abbreviated as CoSe/CdSSe for convenience.

3.2.2. Structure, morphology and composition of TMCoSe/CdSSe NCs

The crystalline phases of the TMCoSe/CdSSe NCs were first investigated by XRD technique. As shown in Fig. 6a, TMCoSe/CdSSe NCs mainly exhibit the typical diffraction peaks of CoSe and CdSSe. Compared with CoSe in CoSe/CdSSe NCs, the intensity of partial diffraction peaks of CoSe in TMCoSe/CdSSe NCs was slightly reduced, which may be due to the regulation of CoSe growth by the incorporation of transition metal ions. Inductively coupled plasma optical emission spectrometer (ICP-OES) analysis exhibited in Table S2 shows that nearly all of the used TM ions were successfully incorporated into the structure of CoSe NPs. Additionally, element energy mapping results demonstrate the uniform distribution of Mn, Fe, Ni, or Cu species in the

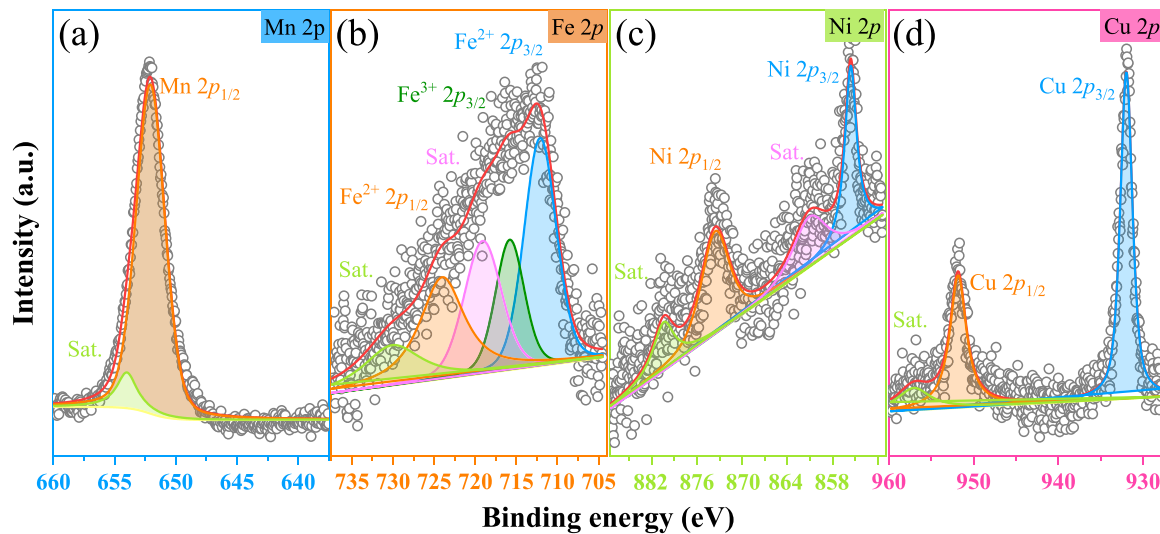


Fig. 7. High-resolution XPS spectra of (a) Mn 2p, (b) Fe 2p, (c) Ni 2p, and (d) Cu 2p for MnCoSe/CdSSe, FeCoSe/CdSSe, NiCoSe/CdSSe, and CuCoSe/CdSSe sample, respectively.

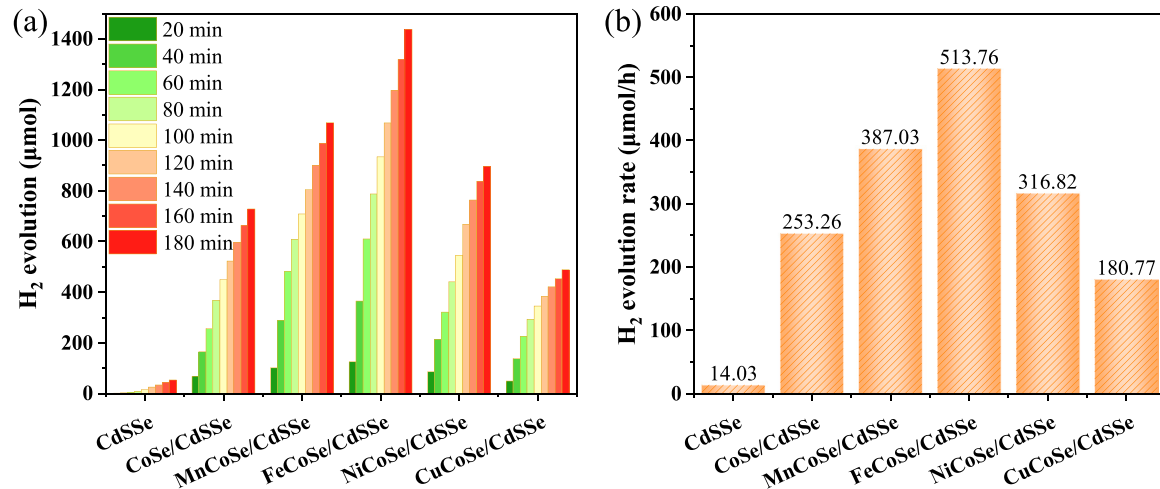


Fig. 8. (a) Reaction time courses and (b) the average rate of H₂ evolution over different photocatalysts in aqueous solution. Reaction conditions: catalyst, 50 mg; 50 mL 1 vol. % lactic acid aqueous solution; light source, 300 W Xenon lamp ($\lambda \geq 420$ nm).

corresponding TMCoSe/CdSSe NC (Fig. S13), indicating TM ions have been uniformly doped into CoSe. Fig. 6b exhibits DRS results of TMCoSe/CdSSe and CoSe/CdSSe NCs. The same cutoff absorption edges can be observed for TMCoSe/CdSSe NCs, CoSe/CdSSe NCs, and CdSSe, signifying TM ions are only incorporated into the lattice of CoSe cocatalyst without affecting its crystal structures.

The surface chemical state of TMCoSe/CdSSe NCs was detected by the XPS technique, and high-resolution XPS spectra are displayed in Fig. S12 and Fig. 7. Specifically, accompanied by a satellite peak (abbreviated as 'sat.'), the peak centered at 652.1 eV corresponds to the Mn²⁺ 2p_{1/2} [44] (Fig. 7a). The Fe 2p spectrum can be decomposed into three sub-peaks and two satellite peaks: the characteristic peaks with BEs of 712.1 eV and 724.0 eV belong to Fe²⁺ 2p_{3/2} and Fe²⁺ 2p_{1/2} spin-orbits, respectively [45] (Fig. 7b), and the signal at 715.8 eV can be assigned to Fe³⁺ 2p_{3/2} [46], which may be originated from the partially oxidized Fe species. Similarly, the Ni 2p spectrum can be fitted by four peaks including two satellite peaks, in which the two deconvolution peaks with BEs of 855.6 eV and 873.5 eV are attributed to Ni²⁺ 2p_{3/2} and Ni²⁺ 2p_{1/2}, respectively [47] (Fig. 7c). For Cu 2p spectrum, the two strong peaks centered at 932.0 eV (2p_{3/2}) and 951.8 eV (2p_{1/2}) (Fig. 7d) with a standard separation of 19.8 eV confirm the monovalent copper in

CuCoSe [48]. The above results indicate that these four metal elements are presented in the samples in ionic form rather than TM clusters. This can be further confirmed by Raman analysis, in which no TM metal bonds were observed as exhibited in Fig. S14. Moreover, compared with CdSSe NWs and CoSe, the BEs of Cd 3d and S 2p of TMCoSe/CdSSe NCs shift positively, while Se 3d and Co 2p of TMCoSe/CdSSe NCs show negative-shift BEs. These shifts reveal that a strong interfacial interaction between TMCoSe and CdSSe is formed, that is the formation of heterojunctions, and TMCoSe modifications cause electrons spontaneously transfer from CdSSe to TMCoSe through the junction interface [14].

3.2.3. Photocatalytic HER activity of TMCoSe/CdSSe NCs

Photocatalytic water splitting activities for H₂ production were evaluated under visible-light irradiation ($\lambda \geq 420$ nm). Fig. 8a displays photocatalytic cumulative H₂ production over CdSSe, CoSe/CdSSe, and TMCoSe/CdSSe NCs. Obviously, the HER activity of FeCoSe/CdSSe NC is superior to other photocatalysts. Specifically, CdSSe and CoSe/CdSSe only give 52.8 μmol and 729.2 μmol H₂ after 180 min of irradiation, respectively, while 1069.4 μmol, 896.8 μmol and 488.8 μmol H₂ can be detected after 180 min of irradiation over MnCoSe/CdSSe, NiCoSe/

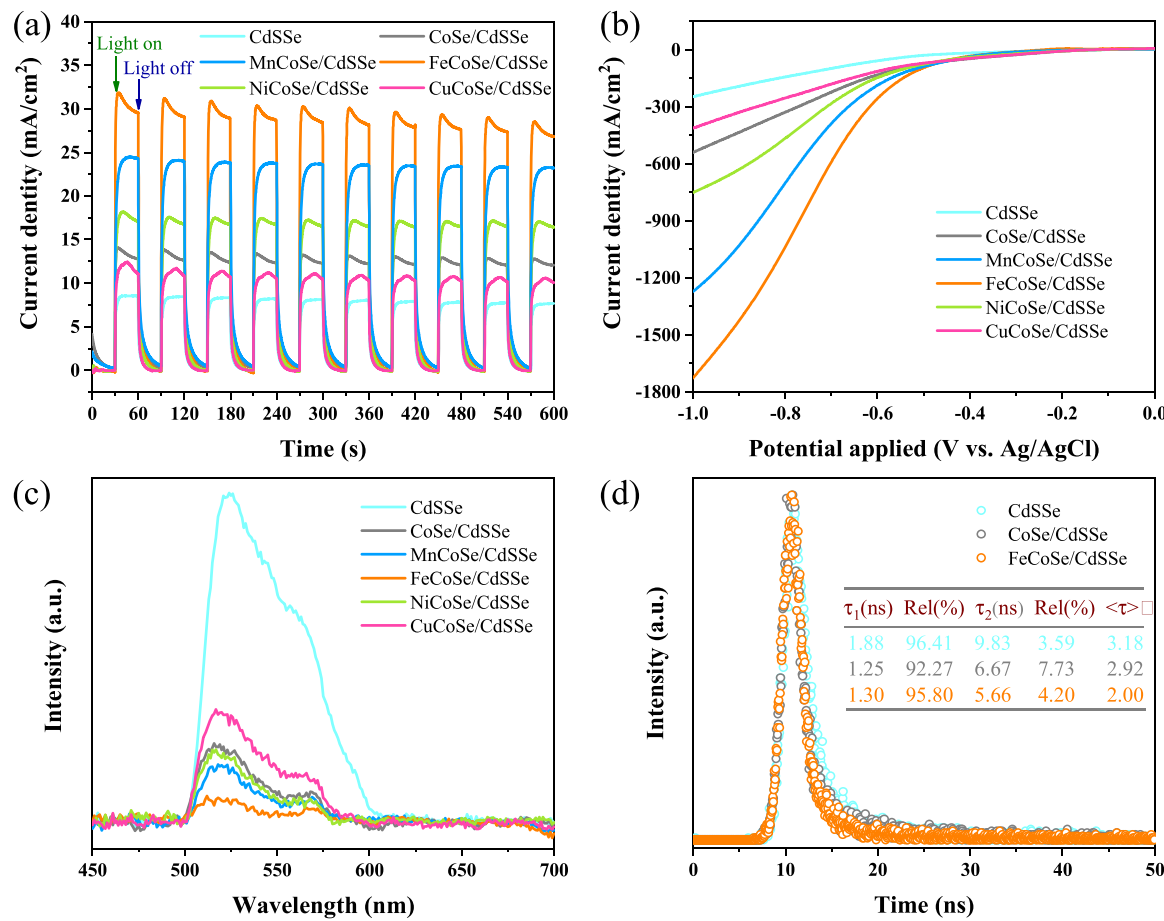


Fig. 9. (a) Transient photocurrent-time curves, (b) Linear Sweep Voltammetry and (c) Time-resolved PL decay spectra of CdSSe, CoSe/CdSSe and FeCoSe/CdSSe, respectively. (d) photoluminescence spectra of the as-prepared samples. Electrolyte: 0.1 M Na_2SO_4 solution; light source, 300 W Xenon lamp ($\lambda \geq 420$ nm).

CdSSe and CuCoSe/CdSSe samples, respectively. Notably, compared with CoSe/CdSSe, the H_2 activities of those nanocomposites doped with Mn, Fe and Ni ions are enhanced, but that of the CuCoSe/CdSSe is attenuated. This may be owing to the effect of doped Cu^{2+} in CuCoSe, which leads to a feeble charge separation capacity (lower ΔV) and sluggish surface reaction kinetics (higher ΔG_{H^*}), as demonstrated by DFT investigations above. Fig. 8b presents the H_2 evolution rate of CdSSe, CoSe/CdSSe and TMCoSe/CdSSe NCs. It can be seen that FeCoSe/CdSSe NC exhibits the highest H_2 formation rate (513.76 $\mu\text{mol h}^{-1}$), which is 36.6 times and 2.0 times higher than that of CdSSe and CoSe/CdSSe, respectively. Therefore, it is evidenced that the intrinsic properties of CoSe cocatalyst have been modified after introducing the TM heteroatoms, especially Fe atoms, thus resulting in improved photocatalytic HER activities over CdSSe-based semiconductors.

3.2.4. Carrier dynamics analysis of TMCoSe/CdSSe NCs

The electrochemically active surface areas (ECSA) of the various samples (Fig. S15) were estimated to assess the influence of electrochemically accessible active sites on photocatalytic HER activities. The similar ECSA values mean that the electrochemically accessible active sites do not play key roles in improving the photocatalytic HER activities over TMCoSe/CdSSe samples, which indicate that their superior activities maybe rely on the excellent carrier dynamics during photocatalytic reactions. To clarify the underlying effects of heteroatom doping on the carrier dynamics of CdSSe, several photoelectrochemistry investigations of the obtained samples were carried out. In electrochemical impedance spectroscopy (EIS) Nyquist plots (Fig. S16), the FeCoSe/CdSSe sample exhibits a smaller semicircle compared with other electrodes, indicating a faster charge transfer rate in FeCoSe/CdSSe. Fig. 9a gives the

photocurrent response of each electrode. Note that the photocurrent over FeCoSe/CdSSe NC electrode is distinctly enhanced compared with that of other electrodes. Generally, photocurrent is mainly formed by the diffusion of photoinduced electrons to the back electrode substrate, meanwhile the holes are consumed by hole acceptors in the electrolyte [49]. The improved photocurrent over FeCoSe/CdSSe NCs signifies a high separation efficiency ($\eta_{\text{charge separation}}$) of photogenerated electron-hole pairs, which is in consistent with the DFT calculations mentioned above. The electrochemical H_2 evolution performances of CdSSe, CoSe/CdSSe and TMCoSe/CdSSe electrodes were also measured by the linear sweep voltammetry (LSV) method. Basically, the photocatalytic H_2 evolution activity is highly dependent on the overpotential of HER [50]. Fig. 9b exhibits the overpotential of each electrode. It can be seen that FeCoSe/CdSSe has the lowest value among these samples, suggesting it is a preeminent photocatalyst for HER. This may benefit from the excellent ΔG_{H^*} (high $\eta_{\text{surface reaction}}$) of FeCoSe cocatalyst as analyzed based on DFT investigations.

Steady-state photoluminescence (PL) spectra were conducted to further explore information on the migration, separation, and trapping process of photogenerated electron-hole pairs. Generally, weak PL intensity means a high electron-hole pairs separation rate [51]. Fig. 9c shows the PL spectra of all samples under the excitation wavelength of 380 nm. Two distinct emission bands at about 520 and 569 nm are observed, which can be ascribed to the band gap emission and surface recombination of electrons and holes, respectively [14]. When TMCoSe cocatalysts are loaded onto CdSSe, the peak intensity of CdSSe emission is drastically quenched. Besides, the PL intensity of FeCoSe/CdSSe is lower than that of other samples, indicating FeCoSe/CdSSe has the highest separation rate of photogenerated electron-hole pairs among all

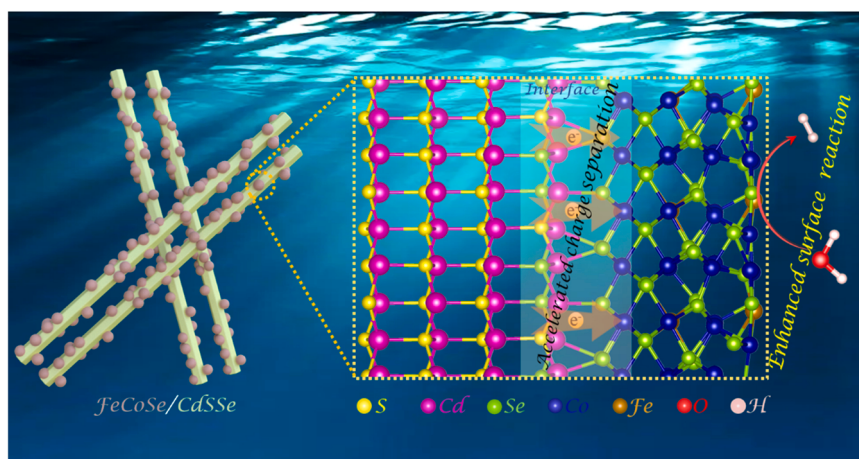


Fig. 10. Proposed mechanism for photocatalytic H_2 evolution over FeCoSe/CdSSe sample.

samples. The transfer of photogenerated charge carriers of these samples has also been confirmed by time-resolved photoluminescence (TRPL) spectra. As shown in Fig. 9d, the significantly decreased lifetime of FeCoSe/CdSSe (2.00 ns) compared with that of CoSe/CdSSe (2.92 ns) and CdSSe (3.18 ns) indicates FeCoSe is an effective cocatalyst for charge transfer, which can suppress the electron-hole recombination efficiently [52]. The facilitated separation of photogenerated charge carriers in FeCoSe/CdSSe gives electrons more opportunities for participating the subsequent HER process, thus enhancing photocatalytic efficiency.

Based on the aforementioned theoretical and experimental investigations, a possible mechanism for the improved photocatalytic H_2 generation over TMCoSe/CdSSe sample (taking FeCoSe/CdSSe as an example) was proposed as shown in Fig. 10. Since the original W_F of CdSSe (4.45 eV) is smaller than that of FeCoSe (4.84 eV), the intimate contact between CdSSe and FeCoSe in FeCoSe/CdSSe leads to the electron transfer from CdSSe to FeCoSe, accompanied by the bent “upward” of the CB and VB of CdSSe. As a result, the Schottky junctions are constructed between CdSSe and FeCoSe, which can serve as an electron trap to efficiently capture the photogenerated electrons and prevent them returning to CdSSe under visible light irradiation. Moreover, FeCoSe cocatalyst can further promote the electrons transfer to its surface due to its remarkable conductivity, and then triggers water reduction efficiently to generate H_2 gas because of its high-efficiency catalytic H_2 production activity.

4. Conclusions

In summary, the electronic structure properties of CoSe, TMCoSe, and TMCoSe/CdSSe nanocomposite were investigated by DFT calculations first. Calculated results demonstrate that doping foreign TM elements has distinct effects on the electronic structures of CoSe and CoSe/CdSSe Schottky heterojunction. Among them, FeCoSe can efficiently accelerate electron-hole pairs separation and improve surface HER efficiency, benefitted by the large potential drop (ΔV) and the reduced Gibbs free energy of hydrogen adsorption (ΔG_H^*), which may potentially permit an enhanced photocatalytic efficiency. Subsequently, based on the theoretical predictions, 0D/1D structured TMCoSe/CdSSe nanocomposite was fabricated via the solvothermal method for water splitting under visible-light irradiation. And their photocatalytic H_2 activities are obviously different. Particularly, FeCoSe/CdSSe photocatalyst exhibits the most excellent photocatalytic HER performance ($513.76 \mu\text{mol h}^{-1}$), which is 36.6 times and 2.0 times higher than that of pure CdSSe and the optimal CoSe/CdSSe, respectively. In addition, the carrier dynamics investigations reveal that FeCoSe/CdSSe shows the most rapid charge separation efficiency and migration rate among all

samples. All the experimental results are in good consistent with the theoretical study results. This work demonstrates the great advantage of using modern theoretical tools for the rational design of novel catalysts for photocatalytic reactions.

CRediT authorship contribution statement

Shiwen Du: Investigation, Theoretical calculation, Writing. **Shengqi Lin:** Performing experiments, Data curation. **Kuankuan Ren:** Editing, Software, Project administration. **Chunhe Li:** Writing, Reviewing, Formal analysis, Project administration. **Fuxiang Zhang:** Conceptualization, Supervision, Visualization.

Declaration of Competing Interest

The authors declare that they have no known competing financial interests or personal relationships that could have appeared to influence the work reported in this paper.

Data availability

Data will be made available on request.

Acknowledgments

This work was financially supported by the Natural Science Foundation of Zhejiang Province, China (Grant No. LQ21B030005 and LQ22A040001), Postdoctoral Science Foundation, China (No. 2021M692459 and 2022M723283), and the National Natural Science Foundation of China (Grant No. 12204313).

Appendix A. Supporting information

Supplementary data associated with this article can be found in the online version at doi:10.1016/j.apcatb.2023.122503.

References

- [1] T. Hisatomi, K. Domen, *Nat. Catal.* 2 (2019) 387–399.
- [2] X. Tao, Y. Zhao, S. Wang, C. Li, R. Li, *Chem. Soc. Rev.* 51 (2022) 3561–3608.
- [3] A. Fujishima, K. Honda, *Nature* 238 (1972) 37–38.
- [4] B. Dong, J. Cui, T. Liu, Y. Gao, Y. Qi, D. Li, F. Xiong, F. Zhang, C. Li, *Adv. Energy Mater.* 8 (2018) 1801660.
- [5] J.K. Stolarczyk, S. Bhattacharyya, L. Polavarapu, J. Feldmann, *ACS Catal.* 8 (2018) 3602–3635.
- [6] J. Ran, J. Zhang, J. Yu, M. Jaroniec, S.Z. Qiao, *Chem. Soc. Rev.* 43 (2014) 7787–7812.
- [7] Q. Zhu, Z. Xu, B. Qiu, M. Xing, J. Zhang, *Small* 17 (2021) 2101070.

- [8] H. Zhao, L. Jian, M. Gong, M. Jing, H. Li, Q. Mao, T. Lu, Y. Guo, R. Ji, W. Chi, Y. Dong, Y. Zhu, *Small Struct.* 3 (2022) 2100229.
- [9] B. Liu, Y.-F. Zhao, H.-Q. Peng, Z.-Y. Zhang, C.-K. Sit, M.-F. Yuen, T.-R. Zhang, C.-S. Lee, W.-J. Zhang, *Adv. Mater.* 29 (2017) 1606521.
- [10] D. Gao, W. Zhong, X. Wang, F. Chen, H. Yu, J. Mater. Chem. A 10 (2022) 7989–7998.
- [11] S. Jayachitra, D. Mahendiran, P. Ravi, P. Murugan, M. Sathish, *Appl. Catal. B-Environ.* 307 (2022), 121159.
- [12] S. Du, X. Lin, C. Li, G. Li, B. Zheng, Y. Liu, H. Xu, P. Fang, *Chem. Eng. J.* 389 (2020), 124431.
- [13] D. Zeng, L. Xiao, W.-J. Ong, P. Wu, H. Zheng, Y. Chen, D.-L. Peng, *ChemSusChem* 10 (2017) 4624–4631.
- [14] S. Du, G. Li, X. Lin, S. Zhang, H. Xu, P. Fang, *Chem. Eng. J.* 409 (2021), 128157.
- [15] Z. Chen, H. Gong, Q. Liu, M. Song, C. Huang, *ACS Sustain. Chem. Eng.* 7 (2019) 16720–16728.
- [16] R.M. Irfan, M.H. Tahir, M. Maqsood, Y. Lin, T. Bashir, S. Iqbal, J. Zhao, L. Gao, M. Haroon, *J. Catal.* 390 (2020) 196–205.
- [17] S. Hong, D.P. Kumar, E.H. Kim, H. Park, M. Gopannagari, D.A. Reddy, T.K. Kim, *J. Mater. Chem. A* 5 (2017) 20851–20859.
- [18] Y. Lei, Y. Zhang, Z. Li, S. Xu, J. Huang, K. Hoong Ng, Y. Lai, *Chem. Eng. J.* 425 (2021), 131478.
- [19] P. Qiu, R. Hu, X. Wang, Y. Xue, J. Tian, X. Chen, *Mater. Chem. Front.* 6 (2022) 718–723.
- [20] X. Meng, W. Qi, W. Kuang, S. Adimi, H. Guo, T. Thomas, S. Liu, Z. Wang, M. Yang, *J. Mater. Chem. A* 8 (2020) 15774–15781.
- [21] G. Kresse, J. Furthmüller, *Phys. Rev. B* 54 (1996) 11169–11186.
- [22] D.J.G. Kresse, *Phys. Rev. B* 59 (1999) 1758–1775.
- [23] P.E. Blöchl, *Phys. Rev. B* 50 (1994) 17953–17979.
- [24] J. Hafner, *J. Comput. Chem.* 29 (2008) 2044–2078.
- [25] J.P. Perdew, J.A. Chevary, S.H. Vosko, K.A. Jackson, M.R. Pederson, D.J. Singh, C. Fiolhais, *Phys. Rev. B* 46 (1992) 6671–6687.
- [26] J.P. Perdew, K. Burke, E. Matthias, *Phys. Rev. Lett.* 77 (1996) 3865–3868.
- [27] H.J. Monkhorst, J.D. Pack, *Phys. Rev. B* 13 (1976) 5188–5192.
- [28] J. Bai, W. Chen, R. Shen, Z. Jiang, P. Zhang, W. Liu, X. Li, *J. Mater. Sci. Technol.* 112 (2022) 85–95.
- [29] Y. Liu, J. Lian, M. Zhao, Y. Wang, M. Li, H. Song, *EPL (Europhys. Lett.)* 117 (2017) 57007.
- [30] D. Gao, X. Wu, P. Wang, H. Yu, B. Zhu, J. Fan, J. Yu, *Chem. Eng. J.* 408 (2021), 127230.
- [31] W. Qiu, P. Lu, X. Yuan, F. Xu, L. Wu, X. Ke, H. Liu, J. Yang, X. Shi, L. Chen, J. Yang, W. Zhang, *J. Chem. Phys.* 144 (2016), 194502.
- [32] J.K. Nørskov, T. Bligaard, A. Logadottir, J.R. Kitchin, J.G. Chen, S. Pandelov, U. Stimming, *J. Electrochem. Soc.* 152 (2005) J23.
- [33] D. Wang, Z.-P. Liu, W.-M. Yang, *ACS Catal.* 7 (2017) 2744–2752.
- [34] H. Cai, B. Wang, L. Xiong, J. Bi, H. Hao, X. Yu, C. Li, J. Liu, S. Yang, *Nano Res* 15 (2022) 1128–1134.
- [35] X. Zhu, Z. Wang, K. Zhong, Q. Li, P. Ding, Z. Feng, J. Yang, Y. Du, Y. Song, Y. Hua, J. Yuan, Y. She, H. Li, H. Xu, *Chem. Eng. J.* 429 (2022), 132204.
- [36] Y. Zhou, J. Zhang, H. Ren, Y. Pan, Y. Yan, F. Sun, X. Wang, S. Wang, J. Zhang, *Appl. Catal. B-Environ.* 268 (2020), 118467.
- [37] C. Zhou, J. Zhou, L. Lu, J. Wang, Z. Shi, B. Wang, L. Pei, S. Yan, Y. Zhentao, Z. Zou, *Appl. Catal. B-Environ.* 237 (2018) 742–752.
- [38] B. Hinnemann, P.G. Moses, J. Bonde, K.P. Jørgensen, J.H. Nielsen, S. Horch, I. Chorkendorff, J.K. Nørskov, *J. Am. Chem. Soc.* 127 (2005) 5308–5309.
- [39] Z. Ye, Y. Jiang, L. Li, F. Wu, R. Chen, *Adv. Mater.* 32 (2020) 2002168.
- [40] F. Wang, Y. Li, T.A. Shifa, K. Liu, F. Wang, Z. Wang, P. Xu, Q. Wang, J. He, *Angew. Chem. Int. Ed.* 55 (2016) 6919–6924.
- [41] Y. Li, Y. Zhao, F.-M. Li, Z. Dang, P. Gao, *ACS Appl. Mater. Inter.* 13 (2021) 34457–34467.
- [42] S. Qiu, X. Liang, S. Niu, Q. Chen, G. Wang, M. Chen, *Nano Res* 15 (2022) 7925–7932.
- [43] J. Du, G. Liu, F. Li, Y. Zhu, L. Sun, *Adv. Sci.* 6 (2019) 1900117.
- [44] Z. Nie, L. Zhang, X. Ding, M. Cong, F. Xu, L. Ma, M. Guo, M. Li, L. Zhang, *Adv. Mater.* 34 (2022) 2108180.
- [45] H. Li, C. Hu, Y. Xia, T. Li, D. Zhang, F. Xu, *Nano Res* 14 (2021) 3952–3960.
- [46] Z. Yang, X. Xu, X. Liang, C. Lei, Y. Wei, P. He, B. Lv, H. Ma, Z. Lei, *Appl. Catal. B-Environ.* 198 (2016) 112–123.
- [47] Z. Wei, M. Guo, Q. Zhang, *Appl. Catal. B-Environ.* 322 (2023), 122101.
- [48] A. Singh, S. Singh, S. Levchenko, T. Unold, F. Laffir, K.M. Ryan, *Angew. Chem. Int. Ed.* 52 (2013) 9120–9124.
- [49] M.D. Ward, A.J. Bard, *J. Phys. Chem.* 86 (1982) 3599–3605.
- [50] J. Tao, M. Wang, X. Zhang, L. Lu, H. Tang, Q. Liu, S. Lei, G. Qiao, G. Liu, *Appl. Catal. B-Environ.* 320 (2023), 122004.
- [51] Z. Wei, W. Wang, W. Li, X. Bai, J. Zhao, E.C.M. Tse, D.L. Phillips, Y. Zhu, *Angew. Chem. Int. Ed.* 60 (2021) 8236–8242.
- [52] Z. Sun, H. Zheng, J. Li, P. Du, *Energ. Environ. Sci.* 8 (2015) 2668–2676.